Article

Magnetic Interactions in Dinuclear MnMn Complexes Covalently Tethered to Organic Radicals: Spectroscopic Models for the SY State of Photosystem II

Dana S. Marlin, Eckhard Bill, Thomas Weyhermller, Eberhard Bothe, and Karl Wieghardt

J. Am. Chem. Soc., **2005**, 127 (16), 6095-6108• DOI: 10.1021/ja042655w • Publication Date (Web): 29 March 2005

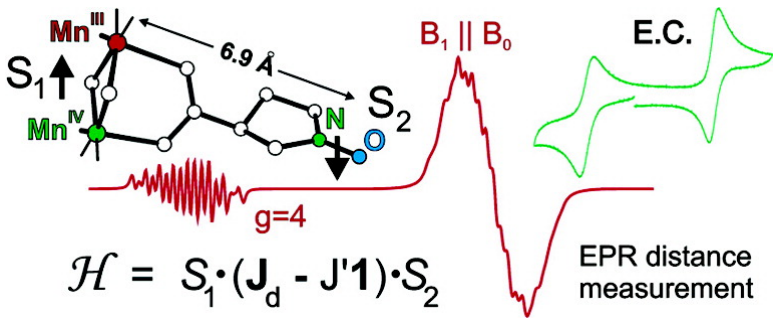

More About This Article

Additional resources and features associated with this article are available within the HTML version:

- Supporting Information
- Links to the 6 articles that cite this article, as of the time of this article download
- Access to high resolution figures
- Links to articles and content related to this article
- Copyright permission to reproduce figures and/or text from this article

View the Full Text HTML

J|A|C|S
ARTICLES
Published on Web 03/29/2005

Magnetic Interactions in Dinuclear $Mn^{III}Mn^{IV}$ Complexes Covalently Tethered to Organic Radicals: Spectroscopic Models for the $S_2Y_z^{\bullet}$ State of Photosystem II

Dana S. Marlin,† Eckhard Bill,* Thomas Weyhermüller, Eberhard Bothe, and Karl Wieghardt*

Contribution from the Max-Planck-Institut für Bioanorganische Chemie, Stiftstrasse 34-36, D-45470 Mülheim an der Ruhr, Germany

Received December 7, 2004; E-mail: bill@mpi-muelheim.mpg.de

Abstract: A series of isostructural dimeric manganese complexes of the type $[(Me_4dtne)Mn_2(\mu\text{-}O)_2(\mu\text{-}R)]^{2+}(X^-)_2$ have been prepared and characterized. The dimanganese cores of these complexes are rigidly held together by the hexadentate ligand Me_4dtne (Me_4dtne = 1,2-bis(4,7-dimethyl-1,4,7-triazacyclonon-1-yl)ethane). Molecular structures for the entire series have been obtained by X-ray diffraction measurements, of which complexes **2** (R = $^-O_2$BPh), **3** (R = $^-O_2$C-PROXYL), **4** (R = $^-O_2$C-TEMPO), and **5** (R = $^-O_2$BPhNIT) are reported here (HO_2C-PROXYL = 3-carboxy-2,2,5,5-tetramethylpyrrolidin-1-yloxy; HO_2C-TEMPO = 4-carboxy-2,2,6,6-tetramethylpiperidin-1-yloxy; and HO_2BPhNIT = 2-(4-(dihydroxyboranyl)-phenyl)-4,4,5,5-tetramethyl-3-oxyimidazolidin-1-oxide). The structures of **1** (R = $^-$OAc) and **6** (R = $^-O_2$CPhNIT) have been reported previously (HO_2CPhNIT = 2-(4-carboxyphenyl)-4,4,5,5-tetramethyl-3-oxyimidazolidin-1-oxide). All complexes exhibit several redox states, which have been investigated by electrochemistry. Complexes **1**, **3**, **4**, and **6** contain a mixed-valent $Mn^{III}Mn^{IV}$ core with an isolated magnetic ground state of $S = 1/2$. The exchange coupling between the manganese ions is strong throughout the series ($J \approx -130 \pm 10$ cm^{-1}, $H = -2JS_1S_2$). The radical complexes **3**, **4**, and **6** exhibit, in addition, long-range exchange interaction (6.9, 7.7, and 8.8 Å, respectively) between the organic radical and the dimanganese core. The intramolecular anisotropic coupling was determined from cw-EPR line shape analyses at S-, X-, and Q-band frequencies and from the intensity of half-field signals detected in normal- and parallel-mode ($J_{d,z} = -120 \times 10^{-4}$, -105×10^{-4}, and -140×10^{-4} cm^{-1}, for **3**, **4**, and **6** respectively). Distance information was obtained for the dimanganese core and the organic radicals from these values by using a three-spin dipole model and local spin contributions for the manganese ions.

Introduction

Electron paramagnetic resonance (EPR) techniques provide powerful tools for measuring metric parameters between paramagnetic centers. The majority of biological applications for distance measurement are performed with artificial spin probes such as spin labels that have been attached chemically or genetically via modified peptide residues carrying nitroxyl radicals.[1] However, the paramagnetic sites in natural systems can also be physiologically available transition metal ions, and in some cases organic radicals that have been somehow stabilized in the reaction cycle of an enzyme. In such cases, EPR investigations of metalloproteins and redox enzymes may yield important and selective structural data, as well as magnetic and electronic information relating to functional sites. These unique and attractive applications, together with the profusion of new metallo-radical enzymes, create many opportunities for interesting EPR distance measurements on bioinorganic systems.[1−3] Through-space dipole interactions of paramagnetic centers are strongly distance dependent and may affect line shapes of continuous wave (CW) EPR spectra, induce "forbidden" half-field transitions, and influence spin relaxation times and EPR pulse responses. Which of these phenomena are dominating and best used for distance measurements depends on the actual separation of the paramagnets and the intrinsic relaxation times of the spin probes and their mobility.[1,4−7] In this contribution we address the problem of fast relaxing spin systems with metal ions possessing large hyperfine interactions and long-distance coupling to covalently linked organic radicals. These systems are best suited for study by using CW-EPR techniques.

One area of biophysical research for which distance measurement by EPR techniques has received healthy usage concerns a long-distance magnetic interaction between tyrosyl radical $Y_z^{\bullet}$

† Present address: School of Chemistry, The University of Edinburgh, Edinburgh, Scotland.

(1) Berliner, L. J., Eaton, S. S., Eaton, G. R., Eds. *Distance Measurements in Biological Systems by EPR*; Kluwer Academic, Plenum Publishers: NewYork, 2000; Vol. 19.
(2) Stubbe, J.; Donk, W. A. v. d. *Chem. Rev.* **1998**, *98*, 705−762.
(3) Houseman, A. L. P.; Doan, P. E.; Goodin, D. B.; Hoffman, B. *Biochemistry* **1993**, *32*, 4430−4443.
(4) Pilbrow, J. R. *Transition Ion Electron Paramagnetic Resonance*; Clarendon Press: Oxford, 1990.
(5) Smith, T. D.; Pilbrow, J. R. *Coord. Chem. Rev.* **1974**, *12*, 173−278.
(6) Eaton, G. R.; Eaton, S. S. *Acc. Chem. Res.* **1988**, *21*, 107.
(7) Eaton, S. S.; Eaton, G. R. *Coord. Chem. Rev.* **1988**, *83*, 29−72.

and the manganese cluster at the reaction center (RC) of Photosystem II (PSII) in the $S_2Y_z^\bullet$ state. The S_2 state is the third of five discrete steps in the catalytic cycle of PSII (labeled S_0-S_4), in which the Mn_4 cluster has an overall spin ground state $S = 1/2$ and shows a multiline EPR spectrum that resembles that of an antiferromagnetically (AF) coupled $Mn^{III}-Mn^{IV}$ dimer.[8−18] Detailed analyses of this state provide evidence that a strong antiferromagnetic interaction exists between three Mn^{III} and a Mn^{IV} ion of the cluster.[16,19,20] The oxidation of the RC to the S_3 state can be blocked, and an intermediate state with a tyrosyl radical $Y_z^\bullet$ can be artificially stabilized, which has been labeled $S_2Y_z^\bullet$. The tyrosine/tyrosyl radical switch at Y_z has been proposed as the first link in the electron transfer chain of events at the RC, and therefore, accurate knowledge of the distance and the type of interaction between these two paramagnetic centers has important consequences relating to the mechanism of electron transfer in PSII. Although X-ray diffraction data from the RC place the Mn_4 and Y_z at 7.5 Å apart,[21−24] the separation of these moieties in the $S_2Y_z^\bullet$ state is unknown. Extensive EPR investigations on $S_2Y_z^\bullet$ have shown the presence of weak, long-range magnetic interactions between the manganese cluster ($S = 1/2$) and $Y_z^\bullet$ ($S' = 1/2$).[9,10,13,14,19]

Although a substantial amount of complexes that contain metal−radical interactions have been assembled in solution and studied by EPR techniques,[4,25−27] there are only a select few that have also been accompanied by structural characterization and so far none that mimics both a strong manganese−manganese exchange (analogous to the manganese cluster in PSII) and a weak manganese−radical coupling (similar to that between the manganese cluster and $Y_z^\bullet$ in $S_2Y_z^\bullet$) within the same complex. We have recently published a communication wherein we report the first such model complex containing an AF coupled $Mn^{III}Mn^{IV}$ ($S = 1/2$) dimer tethered to an organic radical at a distance of 9 Å from the manganese core (complex **6**, Chart 1).[28] We have characterized this complex by a variety of techniques and have also demonstrated the use of dual-mode X-band EPR, as well as SQUID magnetic measurements, to identify the spin ground state for **6** and determine the exchange and dipolar coupling interactions between the radical and manganese cluster. In our earlier interpretation of the EPR spectra for this complex we mentioned some complications, which we address in more detail here.

Chart 1. Overview of the $[(Me_4dtne)Mn_2(\mu\text{-}O)_2(\mu\text{-}R)]^{2+}$ Dications **1**−**6**[a]

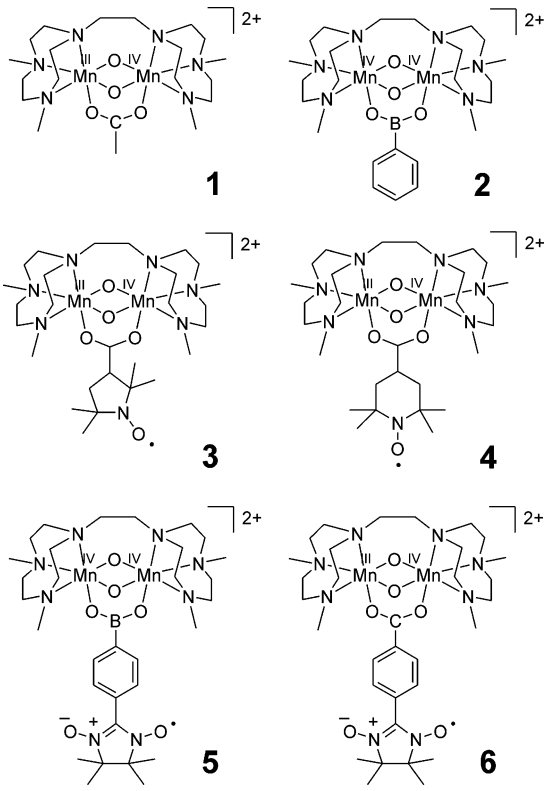

[a] Me_4dtne = 1,2-bis(4,7-dimethyl-1,4,7-triazacyclonon-1-yl)-ethane; R = $^-$OAc (**1**), ^-O_2BPh (**2**), $^-O_2C-$PROXYL (**3**), $^-O_2C-$TEMPO (**4**), $^-O_2BPhNIT$ (**5**), and $^-O_2CPhNIT$ (**6**).

In this work we present a series of dimanganese complexes **1**−**6** that feature the same isostructural dimanganese core rigidly held together by a redox-innocent hexadentate ligand framework (Chart 1). Complexes **3**, **4**, and **6** form a series of complexes with strongly AF coupled $Mn^{III}Mn^{IV}$ ($S = 1/2$) cores tethered to different organic radical ligands. The complete series encompasses various strengths of through-space and through-bond magnetic coupling interactions and also features variations in the orientation and rhombicity between the two coupled paramagnetic entities. Here we present a detailed analysis of the EPR spectra for the series (**1**−**6**) and discuss the methodology for differentiating between, and determining precise, dipolar-coupling and exchange-coupling tensors from the CW-EPR data. All species have been structurally characterized by X-ray crystallography. The electrochemistry and magnetism for all complexes, as well as the experimental and calculated dual-mode X-band and perpendicular mode S-band and Q-band EPR data for complexes **2**−**6**, are presented and discussed. Distance information was calculated for the radical complexes **3**, **4**, and **6** from a three-center dipole model by interpretation of the anisotropic coupling constants on the basis of local spin

(8) Boussac, A.; Zimmermann, J.-L.; Rutherford, A. W. *Biochemistry* **1989**, *28*, 8994−8989.
(9) Dorlet, P.; Boussac, A.; Rutherford, A. W.; Un, S. *J. Phys. Chem. B* **1999**, *103*, 10945−10954.
(10) Dorlet, P.; Valentin, M. D.; Babcock, G. T.; McCracken, J. L. *J. Phys. Chem. B* **1998**, *102*, 8239−8247.
(11) Fiege, R.; Zweygart, W.; Bittl, R.; Adir, N.; Renger, G.; Lubitz, W. *Photosyn. Res.* **1996**, *48*, 227−237.
(12) Hoganson, C. W.; Babcock, G. T. *Science* **1997**, *277*, 1953−1956.
(13) Lakshmi, K. V.; Eaton, S. S.; Eaton, G. R.; Brudvig, G. W. *Biochemistry* **1999**, *38*, 12758−12767.
(14) Lakshmi, K. V.; Eaton, S. S.; Eaton, G. R.; Frank, H. A.; Brudvig, G. W. *J. Phys. Chem. B* **1998**, *102*, 8327−8335.
(15) Lubitz, W.; Lendzian, F.; Bittl, R. *Acc. Chem. Res.* **2002**, *35*, 313−320.
(16) Peloquin, J. M.; Campbell, K. A.; Britt, R. D. *J. Am. Chem. Soc.* **1998**, *120*, 6840−6841.
(17) Szalai, V. A.; Kuhne, H.; Lakshmi, K. V.; Brudvig, G. W. *Biochemistry* **1998**, *37*, 13594−13603.
(18) Tang, X. S.; Randall, D. W.; Force, D. A.; Diner, B. A.; Britt, R. D. *J. Am. Chem. Soc.* **1996**, *118*, 7638−7639.
(19) Horner, O.; Riviere, E.; Blondin, G.; Un, S.; Rutherford, A. W.; Girerd, J. J.; Boussac, A. *J. Am. Chem. Soc.* **1998**, *120*, 7924−7928.
(20) Blondin, G.; Davydov, R.; Philouze, C.; Charlot, M. F.; Styring, S.; Akermark, B.; Girerd, J. J.; Boussac, A. *J. Chem. Soc., Dalton Trans.* **1997**, 4069−4074.
(21) Ferreira, K. N.; Iverson, T. M.; Maghlaoui, K.; Barber, J.; Iwata, S. *Science* **2004**, *303*, 1831−1838.
(22) Kamiya, N.; Shen, J. R. *Proc. Natl. Acad. Sc.i. U.S.A.* **2003**, *100*, 98−103.
(23) Zouni, A.; Witt, H. T.; Kern, J.; Fromme, P.; Krauss, N.; Saenger, W.; Orth, P. *Nature* **2001**, *409*, 739−743.
(24) Rutherford, A. W.; Boussac, A. *Science* **2004**, *303*, 1782−1784.
(25) Eaton, S. S.; More, K. M.; Sawant, B. M.; Boymel, P. M.; Eaton, G. r. *J. Magn. Reson.* **1983**, *52*, 435−449.
(26) More, K. M.; Eaton, G. R.; Eaton, S. S. *Can. J. Chem.* **1982**, *60*, 1392−1401.
(27) More, K. M.; Eaton, G. R.; Eaton, S. S. *J. Magn. Reson.* **1985**, *63*, 151−167.
(28) Marlin, D. S.; Bill, E.; Weyhermüller, T.; Rentschler, E.; Wieghardt, K. *Angew. Chem., Int. Ed.* **2002**, *41*, 4775−4779.

Table 1. Crystallographic Data for **2**·$(PF_6)_2$·toluene, **3**·$(BPh_4)_2$·MeCN, **4**·$(ClO_4)_2$, and **5**·$(ClO_4)_2$

	2·$(PF_6)_2$·toluene	**3**·$(BPh_4)_2$·MeCN	**4**·$(ClO_4)_2$	**5**·$(ClO_4)_2$
chem formula	$C_{31}H_{53}BF_{12}Mn_2N_6O_4P_2$	$C_{77}H_{98}B_2Mn_2N_8O_5$	$C_{28}H_{57}Cl_2Mn_2N_7O_{13}$	$C_{31}H_{58}BCl_2Mn_2N_8O_{15}$
fw	984.42	1347.13	880.59	974.44
space group	*P*2/*c*, No. 13	$P\bar{1}$, No. 2	*Pnma*, No. 62	$P\bar{1}$, No. 2
a, Å	22.0188(11)	12.6006(4)	17.0472(6)	11.311(2)
b, Å	10.7399(4)	13.6769(6)	12.1525(4)	12.638(2)
c, Å	17.5903(9)	23.4457(8)	18.6112(6)	16.855(3)
α, deg	90	73.87(1)	90	101.11(2)
β, deg	102.75(1)	84.33(1)	90	108.28(2)
γ, deg	90	65.24(1)	90	103.46(2)
V, Å	4057.2(3)	3524.0(2)	3855.6(2)	2130.9(6)
Z	4	2	4	2
T, K	100(2)	100(2)	100(2)	100(2)
ρ_{calcd}, g cm^{-3}	1.612	1.270	1.517	1.519
no. of reflns collected/$2\theta_{max}$	40 733/60.00	50 960/52.00	83 858/54.98	9889/45.00
no. of unique reflns/$I>2\sigma(I)$	11761/8380	13853/10491	4635/3949	5411/3297
no. of params/restraints	634/401	856/0	234/112	541/0
μ(Mo Kα), cm^{-1}	8.01	4.15	8.62	7.92
R1[a]/goodness of fit[b]	0.0526/1.014	0.0740/1.077	0.0483/1.043	0.0912/1.097
WR2[c] ($I>2\sigma(I)$)	0.1090	0.1807	0.1159	0.1769

[a] Observation criterion: $I > 2\sigma(I)$. $R1 = \sum||F_o| - |F_c||/\sum|F_o|$. [b] $GooF = [\sum[w(F_o^2 - F_c^2)^2]/(n-p)]^{1/2}$. [c] $wR2 = [\sum[w(F_o^2 - F_c^2)^2]/\sum[w(F_o^2)^2]]^{1/2}$ where $w = 1/\sigma^2(F_o^2) + (aP)^2 + bP$, $P = (F_o^2 + 2F_c^2)/3$.

Chart 2. Schematic View of the Ligands

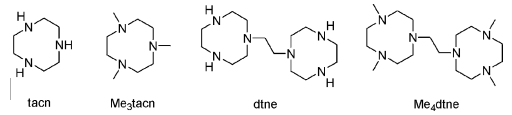

densities[29] for the mixed-valence $Mn^{III}Mn^{IV}$ cores. Finally, the implications, both structural and magnetic, from this series of model complex studies are discussed in the context of their relation to the $S_2Y_z^{\bullet}$ state of PSII.

Experimental Section

The synthesis of complexes **2**−**5** and information pertaining to X-ray data and refinement of the structures are included as Supporting Information. Crystallographic data of the complexes are listed in Table 1. Information regarding the experimental conditions and equipment and software used in collecting and calculating data for magnetic and EPR measurements, as well as for the electrochemical and coulometric measurements, are also found in the Supporting Information.

Results and Discussion

Syntheses of Complexes. Complexes **1**−**6** are derivatives of the common isostructural $[Me_4dtneMn_2(\mu\text{-}O)_2]^{2+/3+}$ core. The hexadentate ligand Me_4dtne provides the rigid framework necessary for maintaining this isostructural dimanganese core and prevents formation of various other manganese-oxo clusters, as have been isolated with the parent ligand systems tacn, Me_3tacn, and dtne (Chart 2).

The syntheses of **1** and **6** have been described elsewhere.[28,30] Complex **2** comprises a $[Me_4dtneMn^{IV}_2(\mu\text{-}O)_2]^{3+}$ core bridged by a phenyl boronato ligand. In **2**, $[Mn^{II}(acetate)_2(H_2O)_4]$ was used as the source of manganese, which was subsequently oxidated to Mn^{IV}. Oxidation of Mn^{II} to Mn^{IV} was achieved at low temperature with the strong base/oxidant mixture of NaOH (2 equiv)/H_2O_2 (30%) in aqueous solution. In the case of the boronato complex **5**, which has a nitronyl nitroxide (NIT) moiety attached to the phenyl boronate ligand, the above oxidation conditions are too harsh and result in decomposition of the NIT moiety. In this case, a milder protocol was used by employing Mn^{III} acetate $[(H_2O)_3Mn^{III}_3(\mu_3\text{-}O)(\mu\text{-}OAc)_6]OAc$ as the Mn source and allowing slow oxidation to Mn^{IV} by air. The enhanced stability provided by the dianionic boronate ligands to Mn^{IV} relative to lower oxidation states (see below) drives the reaction. Although this technique is much slower than that for **2** (72 h vs 30 min), it is nonetheless effective for yielding **5** with intact NIT. The dications **2** and **5** were isolated as their PF_6^- and ClO_4^- salts, respectively. Complexes **3** and **4** where prepared at low temperature with $[Mn^{II}(H_2O)_6](ClO_4)_2$ as the manganese source and 30% H_2O_2 as the oxidant. All syntheses involving H_2O_2 were performed at low temperatures. At room temperature the same reactions resulted in formation of large amounts of intractable brown precipitate (MnO_2) and gave sparingly low yields.

Structures. The solid state structures of all complexes **1**−**6** have been determined by X-ray crystallography. The structures of complexes **1** and **6** have been included in earlier reports,[28,30] while the structures of complexes **2**·$(PF_6)_2$, **3**·$(BPh_4)_2$, **4**·$(ClO_4)_2$, and **5**·$(ClO_4)_2$ are described here.

X-ray quality crystals of $[(Me_4dtne)Mn_2(\mu\text{-}O)_2(\mu\text{-}O_2BPh)](PF_6)_2$, **2**·$(PF_6)_2$, were obtained from CH_3CN/toluene (2:1) solutions of the **2**·$(PF_6)_2$ salt at room temperature over a period of 2 to 3 days. Similarly, X-ray quality single crystals of $[(Me_4dtne)Mn_2(\mu\text{-}O)_2(\mu\text{-}O_2C\text{-}PROXYL)](BPh_4)_2$, **3**·$(BPh_4)_2$, formed upon slow concentration of a CH_3CN/H_2O (1:5) solution of the complex. Large X-ray quality crystals of $[(Me_4dtne)Mn_2(\mu\text{-}O)_2(\mu\text{-}O_2C\text{-}TEMPO)](ClO_4)_2$, **4**·$(ClO_4)_2$, were grown from slow evaporation of an aqueous solution of the complex, while single crystals of $[(Me_4dtne)Mn_2(\mu\text{-}O)_2(\mu\text{-}O_2BPhNIT)](ClO_4)_2$, **5**·$(ClO_4)_2$, were grown from saturated acetonitrile solution of **5** in the presence of excess ClO_4^-. In addition to their isostructural $[Me_4dtneMn_2(\mu\text{-}O)_2]^{2+/3+}$ core, the two Mn centers also have a third bridge, which is either a monoanionic carboxylate in the case of complexes **1**, **3**, **4**, and **6** or a dianionic boronate in the case of complexes **2** and **5**.

The carboxylate bridges are monoanionic ligands and yield mixed-valent $[Me_4dtneMn^{III}Mn^{IV}(\mu\text{-}O)_2(\mu\text{-}O_2CR)]^{2+}$ species, as in **1**, **3**, **4**, and **6**, with localized spins on the $Mn^{III}Mn^{IV}$ centers.

(29) Bertrand, P.; More, C.; Guigliarelli, B.; Fournel, A.; Bennett, B.; Howes, B. *J. Am. Chem. Soc.* **1994**, *116*, 3078−3086..
(30) Schäfer, K. O.; Bittl, R.; Zweygart, W.; Lendzian, F.; Haselhorst, G.; Weyhermüller, T.; Wieghardt, K.; Lubitz, W. *J. Am. Chem. Soc.* **1998**, *120*, 13104−13120.

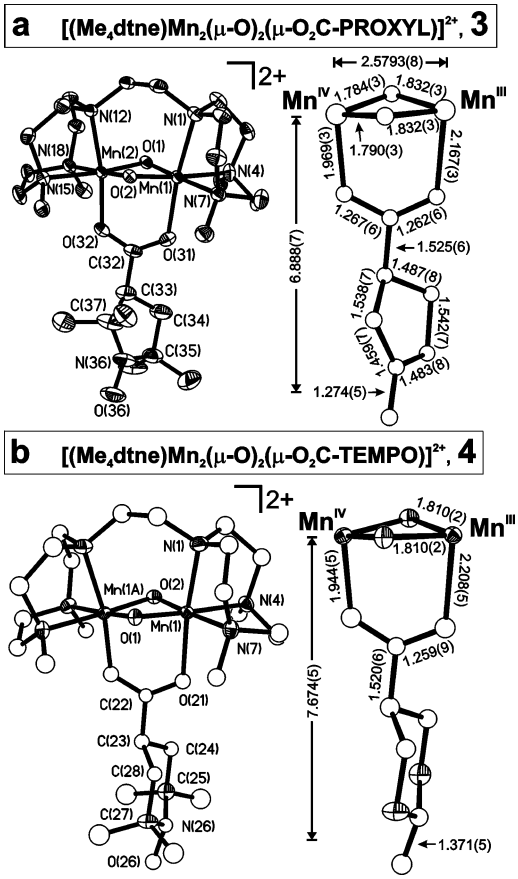

Figure 1. Plot (with ellipsoids at 50% probability) of the crystal structures of the dications of (a) **3** in **3**·$(BPh_4)_2$·MeCN and (b) **4** in **4**·$(ClO_4)_2$. Hydrogen atoms and acetonitrile, BPh_4^-, and ClO_4^- molecules are not shown. Relevant bond distances are included in an expanded section on the right-hand side of each molecule.

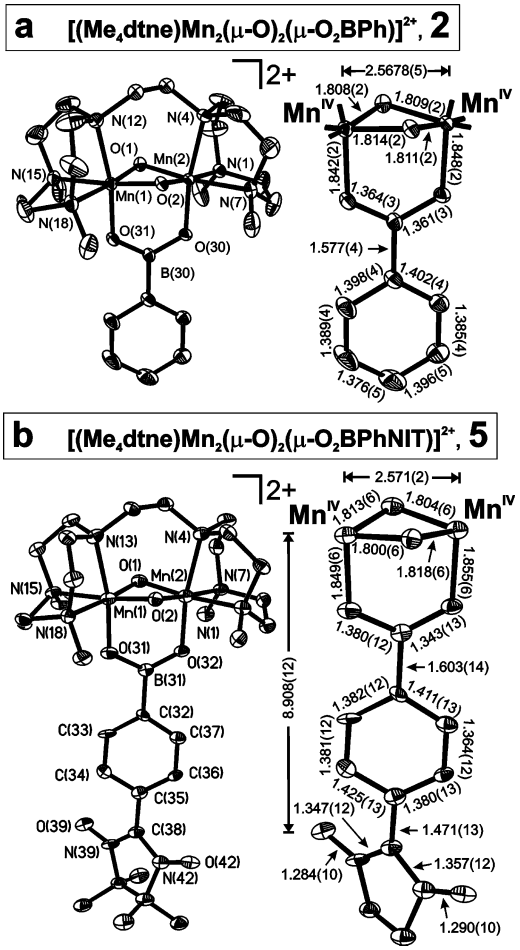

Figure 2. Plot (with ellipsoids at 50% probability) of the crystal structures of the dications of (a) **2** in **2**·$(PF_6)_2$·toluene and (b) **5** in **5**·$(ClO_4)_2$. Hydrogen atoms and toluene, PF_6^-, and ClO_4^- molecules are not shown. Relevant bond distances are included in an expanded section on the right-hand side of each molecule.

The localization of the spins is structurally apparent by the difference in bond lengths around the manganese ions. For Mn^{IV} the Mn−O (where O is oxo or carboxylate) distances in the dimanganese core are shorter than those for the Mn^{III} center and, in addition, the Jahn−Teller axis of the Mn^{III} center is clearly visible in the direction of the $Mn^{III}-O_{carboxylate}$ bond (Figure 1). In contrast, boronates, which are the dianionic analogues of the carboxylates, tend to stabilize a homovalent $Mn^{IV}Mn^{IV}$ core. In complexes **2** and **5** the boronate bridge is bound symmetrically between two Mn^{IV} ions (Figure 2). The Mn−Mn distance in all complexes is on the order of 2.57 Å regardless of the oxidation state of the manganese ions.

The metric distances from the dimanganese core in complexes **3**−**6** to their respective organic radical moiety vary significantly. The shortest manganese cluster to organic radical distance measured for the series is 6.89 Å in complex **3** (measured from the Mn^{IV} ion to the midpoint of the N−O bond of the PROXYL moiety; for the Mn^{III} ion, which carries the majority spin of the dimanganese core, the distance would be 6.99 Å). The distance from the dimanganese core to the midpoint of the N−O bond of the TEMPO moiety in **4** is longer, at 7.67 Å (Figure 1). In the case of complexes **5** and **6**, the distances from the dimanganese core to the midpoint of the nearest N−O bond in the NIT moiety are quite similar, at 8.8−8.9 Å (Figure 2). The range of distances from 6.9 to 8.9 Å for **3**−**6** are well suited for comparison to the estimated distance between the $Y_z^{\bullet}$ radical and the manganese cluster at the RC of PSII (7.5−8.5 Å).

Electrochemistry and Spectro-electrochemistry. The carboxylate-bridged complexes **1**, **3**, **4**, and **6** are isolated in a $Mn^{III}Mn^{IV}$ oxidation state. These species exhibit reversible oxidation and reduction electrochemical processes at approximately 0.28 and −0.75 V vs Fc^+/Fc, corresponding to $Mn^{IV}Mn^{III}/Mn^{IV}Mn^{IV}$ and $Mn^{IV}Mn^{III}/Mn^{III}Mn^{III}$ couples, respectively. The cyclic and square wave voltammograms for **1**, **4**, and **6** are shown in Figure 3. The boronato-bridged complexes **2** and **5** are isolated as $Mn^{IV}Mn^{IV}$ species (see above) and exhibit one reversible reduction process at −0.75 V vs Fc^+/Fc, corresponding to a $Mn^{IV}Mn^{IV}/Mn^{III}Mn^{IV}$ couple (Figure 3). In addition, complexes **3**−**6** are bound to nitroxyl radicals (NIT, TEMPO, or PROXYL), all of which display reversible oxidation processes corresponding to the $[N-O]^{\bullet}/[N{=}O]^+$ couple. For the NIT moiety of **6** this oxidation process occurs at 0.40 V (vs Fc^+/Fc), while for the NIT moiety of **5** the oxidation process is slightly lower, at a potential of 0.33 V (vs Fc^+/Fc). The TEMPO moiety of **4** exhibits an oxidation process at 0.32 V (vs Fc^+/Fc). The oxidation of **3** was obscured by irreversible multielectron oxidation processes of the BPh_4^- counterion in the potential range of the PROXYL and $Mn^{III}Mn^{IV}/Mn^{IV}Mn^{IV}$ couples.

The electrochemical control over the oxidation states of the dimanganese core and also the radical ligand are very useful features of these complexes. Because of the strong AF coupling

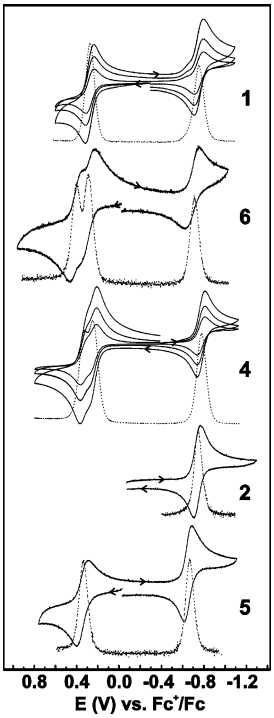

Figure 3. Cyclic (solid lines) and square wave (dashed lines) voltammograms for complexes **1**, **2**, **4**, **5**, and **6**.

between the two Mn ions (see below), this electrochemical control provides a switch between a paramagnetic $Mn^{III}Mn^{IV}$ ($S = 1/2$) core and diamagnetic ($S = 0$) $Mn^{III}Mn^{III}$ or $Mn^{IV}Mn^{IV}$ species. The one-electron reduction of **1** yields a $Mn^{III}Mn^{III}$ core, while oxidation yields a $Mn^{IV}Mn^{IV}$ core. In the case of **2**, the one-electron reduction of the diamagnetic $Mn^{IV}Mn^{IV}$ complex gives rise to a paramagnetic $Mn^{III}Mn^{IV}$ ($S = 1/2$) species which has an EPR spectrum typical of a spin-localized AF coupled $Mn^{III}Mn^{IV}$ core similar to that of **1**. The reversible electrochemical control for **1** and **2**, and the switching between paramagnetic and diamagnetic dimanganese clusters, in combination with electrochemical control over the organic radical ligand (complexes **3**−**6**), is useful for exploring the magnetic properties of these complexes. Controlled-potential coulometry is a convenient means for obtaining complexes **1**−**6** in their various magnetic states.

The cyclic voltammetric and square wave traces for complex **6** corresponding to the reduction and also to the two oxidation processes are shown in Figure 3. At room temperature the two oxidation processes are poorly resolved; however, lowering the temperature to −25 °C narrows the potential range for each process and, in effect, resolves them better. The peak-to-peak potential difference of 0.11 V, which is clearly resolved in the square wave trace (dotted line Figure 3), is sufficient to allow a separation of the oxidation process belonging to the manganese core from that belonging to the NIT moiety. Evidence for the stepwise oxidation of **6** is provided by the distinct spectroelectrochemical changes between the two processes (Figure 4a and b). Controlled potential coulometry at 0.37 V effects oxidation of the $Mn^{III}Mn^{IV}$ core and gives rise to an increase in absorption bands in the high-energy region around 500 nm and concomitant decrease in intensity of the very weak bands in the blue region around 850 nm with an isosbestic point at 765 nm. Changing the potential to 0.82 V results in oxidation of NIT to NIT^+ and a dramatic change in the high-energy

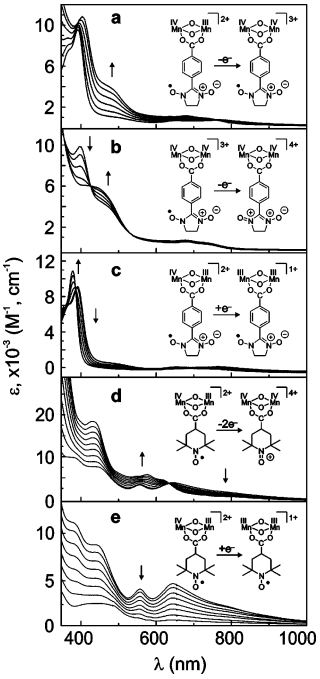

Figure 4. Spectro-electrochemical changes upon (a) first oxidation of **6**, (b) second oxidation of **6**, (c) reduction of **6**, (d) two-electron oxidation of **4**, and (e) reduction of **4**. Controlled potential coulometry experiments were performed on 0.1 mM acetonitrile solutions of the complex with a 1000:1 molar excess of $^tBu_4N{\cdot}PF_6$ as the supporting electrolyte under an argon atmosphere at −25 °C.

absorption bands characterized by a decrease in the intense absorption around 400 nm and an increase in that around 450 nm with an isosbestic point at 425 nm. Subsequent EPR measurements on samples collected after each oxidation confirm that the first oxidation corresponds to a $Mn^{III}Mn^{IV}/Mn^{IV}Mn^{IV}$ process and the second to a NIT/NIT^+ process.

The oxidation and reduction processes for **4** bear resemblance to those for **6** and also feature two overlapping oxidation processes corresponding to the $Mn^{III}Mn^{IV}$ core and the TEMPO radical. However, unlike **6**, they show little temperature dependence down to −30 °C, and no separation of the oxidation belonging to the dimanganese core from that of the TEMPO radical was possible (Figure 4). Our attempts to generate a complex where the dimanganese core is oxidized and the TEMPO radical persists resulted in a two-electron oxidation product of **4** that is EPR silent.

The cyclic voltammetric processes for complexes **2** and **5** are displayed in Figure 3 (bottom). The accompanying spectroelectrochemical changes following the controlled potential coulometric one-electron reduction of complexes **2** and **5** have been included as Supporting Information (Figure S1).

Magnetic Susceptibility. The solid state magnetic properties of all complexes have been measured by temperature- and field-dependent magnetic susceptibility measurements on powdered samples. The magnetic data for $\mathbf{3}{\cdot}(BPh_4)_2$ and $\mathbf{4}{\cdot}(ClO_4)_2$ are included here (Figure 5), while those for $\mathbf{1}{\cdot}(BPh_4)_2$ and $\mathbf{6}{\cdot}(ClO_4)_2$ have been reported elsewhere.[28,30] The magnetic susceptibility data for $\mathbf{2}{\cdot}(PF_6)_2$ and $\mathbf{5}{\cdot}(ClO_4)_2$ are included as Supporting Information (Figure S2). The results of spin-Hamiltonian simulations for all compounds **1**−**6** are summarized in Table 2.

Complexes $\mathbf{3}{\cdot}(BPh_4)_2$ and $\mathbf{4}{\cdot}(ClO_4)_2$ show temperature-independent effective magnetic moments in the range $T = 20-$

Table 2. Spin Hamiltonian Parameters for Compounds **1**−**6**[a]

compound	radical	distance R (Å)	J_{Mn}[b] (cm^{-1})	J'[b] (cm^{-1})	$J_{d,z}$[c] (10^{-4} cm^{-1})	rhombicity ρ[c]
1			−112[d]			
2			−135(5)			
3	PROXYL	6.9	−140(3)	−2.8(4)	−120(5)	0.10(5)
4	TEMPO	7.7	−139(3)	−0.6(4)/0.025(5)[c]	−105(5)	0.5(1)
5			−157(3)			
6	NIT	8.8	−127[e]	−1.1[e]	−140(5)	0.0(1)

[a] The coupling constants J_{Mn} and J' are obtained from simulations with the spin Hamiltonian for three interacting paramagnetic centers: $H = -2J'\,\boldsymbol{S}_{Rad}\cdot(\boldsymbol{S}_{MnIII} + \boldsymbol{S}_{MnIV}) - 2J_{Mn}\,\boldsymbol{S}_{MnIII}\cdot\boldsymbol{S}_{MnIV} + \mu_B\sum \boldsymbol{S}_i\cdot\boldsymbol{g}_i\cdot\boldsymbol{B}$, where $\boldsymbol{S}_{Rad} = 1/2$ is the spin of the PROXYL, TEMPO, or NIT radical, and $S_{MnIII} = 2$ and $S_{MnIV} = 3/2$ are the local spins of the manganese ions for **3**·$(BPh_4)_2$, **4**·$(ClO_4)_2$, and **6**·$(ClO_4)_2$. For simulation of the data from **5**·$(ClO_4)_2$ and the nonradical complexes **1**·$(BPh_4)_2$ and **2**·$(PF_6)_2$ the equation was modified according to the different spin systems (Chart 1). The parameters $J_{d,z}$ and ρ are defined in eq 1; where $\rho = (J_{d,x} - J_{d,y})/J_{d,z}$ is the rhombicity parameter of J_d. The distances R are the shortest separations of the center of the respective radical NO groups from the center of the manganese ions from their molecular structures. [b] Determined from magnetic susceptibility measurements on solid material. [c] Determined from EPR spectra of frozen solutions. [d] Ref 30. [e] Ref 28.

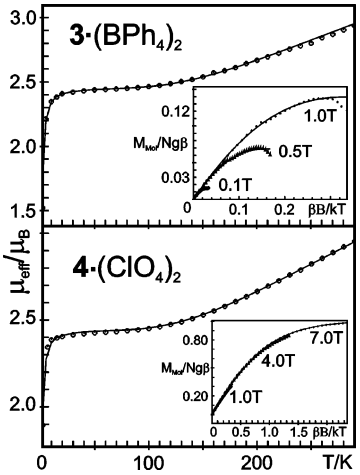

Figure 5. Experimental (•) and calculated (−) temperature-dependent magnetic susceptibility data for complexes **3**·$(BPh_4)_2$ and **4**·$(ClO_4)_2$ (see Table 2). Insets show multiple-field variable-temperature data.

100 K. The data match the spin-only value expected for two (uncoupled) spins $S_1 = S_2 = 1/2$ with $\mu_{eff,s.o.} = \sqrt{2}\cdot g\cdot\sqrt{3/4} = 2.45\ \mu_B$. This reveals dominating strong exchange between the Mn^{III} and Mn^{IV} ions, which yields isolated ground states of the dimanganese cores with "local" subspin $S_{Mn2}{}^0 = 1/2$. The interaction of the dimanganese cores with the tethered radicals ($S_{rad} = 1/2$) is comparatively weak and similar to what was found recently for **6**.[28] Therefore, the magnetic levels arising from the coupling of $S_{Mn2}{}^0$ and S_{rad} are well described as isolated singlet−triplet systems, $|S\rangle$ and $|T\rangle$, which are split by the isotropic part of the long-range exchange interaction. Anisotropic contributions that arise from dipole interaction between the Mn_2 cluster and the radical induce, to first approximation, additional zero-field splitting (zfs) of the triplet state $|T\rangle$.

Spin manifolds with higher "local" subspin $S_{Mn2}{}^n = 3/2$, 5/2, 7/2 for the manganese cores are much higher in energy and are thermally populated only above 120 K, as seen from the increase of the effective magnetic moments $\mu_{eff}(T)$ above this temperature for **3**·$(BPh_4)_2$ and **4**·$(ClO_4)_2$. Spin-Hamiltonian simulations of $\mu_{eff}(T)$ for three interacting sites (see Table 2) yield exchange coupling constants for the $Mn^{III}-Mn^{IV}$ cores of $J_{Mn} = -140$ cm^{-1} for **3**·$(BPh_4)_2$ and -139 cm^{-1} for **4**·$(ClO_4)_2$. The values are fairly similar for all complexes **1**−**6** (Table 2), and for the radical complexes **3**, **4**, and **6** they place the excited spin manifolds at $\Delta \cong 380$ cm^{-1} or higher above the $|S\rangle - |T\rangle$ ground state system ($\Delta = -3J_{Mn}$ for $S_{Mn2}{}^1 = 3/2$). Interestingly, the difference between the (μ-O)$_2$(μ-O_2CR) bridges in complex **1** and the (μ-O)$_2$(μ-O_2BR) bridges in complex **2** is rather marginal, and a similar coupling energy is even found for the homovalent $Mn^{IV}-Mn^{IV}$ motif of complex **5**. This behavior appears to be due to the dominating super exchange pathway via the prevailing (μ-O)$_2$ bridges in the dimanganese cores.

The presence of sizable long-range exchange interaction between the $Mn^{III}Mn^{IV}$ dimers and their respective organic radicals is seen for **3**·$(BPh_4)_2$ and **4**·$(ClO_4)_2$ from the slope of $\mu_{eff}(T)$ below 10 K and, even more clearly, from the nesting of the multiple-field magnetization data shown in the insets of Figure 5. Simulations of the magnetization data, which are particularly sensitive to low-temperature effects due to data sampling on an equidistant $1/T$ scale, yield values for the long-range exchange coupling of $J' = -2.8(\pm0.4)$ cm^{-1} for the solid samples of **3**·$(BPh_4)_2$ and $J' = -0.6(\pm0.4)$ $cm^{-1}$for **4**·$(ClO_4)_2$. For **6**·$(ClO_4)_2$ the value was found[28] to be $-1.1(\pm0.2)$ cm^{-1}. In the present notation as described in Table 2 the value of J' is equal to the singlet−triplet splitting of ground states, Δ_{S-T}.

The zero-field splitting (zfs) of the triplet state due to anisotropic (dipole) coupling is too weak to be probed by static susceptibility data. The metric separations between the $Mn^{III}Mn^{IV}$ cores and the radicals in the range 6.9−8.8 Å yield calculated dipolar interactions on the order of 100×10^{-4} cm^{-1} when a basic point-dipole model is applied. This energy regime is better suited for EPR measurements at low temperatures. Single-ion zfs of the manganese ions was neglected in the present analysis because it only affects the excited spin manifolds with $S > 1/2$, and a measurable influence on the magnetic data could not be detected.

Electron Paramagnetic Resonance. The X-band EPR spectra ($\boldsymbol{B_1}\perp\boldsymbol{B_0}$ and $\boldsymbol{B_1}\|\boldsymbol{B_0}$) for complex **6** were the subject of our previous communication[28] wherein we demonstrated the effectiveness of dual-mode X-band CW-EPR as a tool for obtaining ***g***- and hyperfine ***A***-tensors for the ^{55}Mn centers, as well as anisotropic (dipolar) coupling energies between the Mn_2O_2 core ($S_{Mn2}{}^0 = 1/2$) and the NIT ($S_{rad} = 1/2$) radical. Complexes **3**−**5** were designed in order to alter the pathway of through-bond exchange coupling J' with respect to that of **6** and also to change the effective distance of through-space dipole coupling $\mathbf{J_d}$. From the crystal structure determinations it follows that the complexes **3** and **4** have shorter radical−manganese distances (6.888(7) and 7.674(5) Å respectively) compared to **6** (8.809(2) Å). In addition, the conjugated, through-bond π-pathway for exchange coupling present in **6** has been removed in both cases. We anticipated that complexes **3** and **4** would have an increased dipolar coupling as a result of the shorter

Chart 3. Orientation of the Spectroscopic Principal Axis System with Respect to the Mn_2O_2 Core, and EPR **g** Values and Magnetic Hyperfine Coupling Constants, **A** [in 10^{-4} cm^{-1}] for **1** Adopted from Ref 31

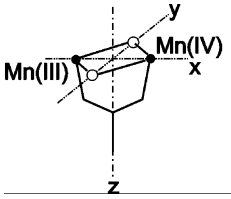

	x	*y*	*z*
G	2.0026	1.9961	1.9830
$\mathbf{A}_{Mn(III)}$	-140.31	-160.89	-104.76
$\mathbf{A}_{Mn(IV)}$	73.90	64.54	72.03

manganese−radical distance compared to **6** and a weaker exchange coupling due to the elimination of the conjugated π-pathway.

Isolated Paramagnetic Centers in Complexes 1 and 5. Complexes **1** and **5** represent magnetically isolated "parent spin" systems of the spin-coupled pairs found in the radical complexes **3**, **4**, and **6**. Complex **1** features the isolated $Mn^{III}Mn^{IV}$($S = 1/2$) core without a tethered organic radical, whereas complex **5** retains a similar but diamagnetic dimanganese core at low temperatures and exhibits paramagnetism arising solely from the NIT radical ($S = 1/2$) moiety. When reduced to a $Mn^{III}Mn^{IV}$ core, **5** retains the same through-space coupling distance between radical and manganese cluster compared to **6**, but has a different through-bond pathway by replacing the carboxylate bridge with boronate.

In a thorough magnetic resonance study on the spectroscopic properties of dimanganese catalase and structurally related model compounds, Schäfer et al. have determined precise EPR **g**-matrixes, ^{55}Mn-hyperfine coupling tensors, and orientation of the magnetic principal axes for several well-characterized synthetic $Mn^{III}Mn^{IV}$ complexes, including complex **1**.[30,31] We use their results as a starting point for our present analysis of Mn_2−radical interactions. In fact, the **g**- and **A**-values calculated for complex **1** (Chart 3) also suitably describe the dimanganese cores of complexes **3**, **4**, and **6**. For the spin-coupled systems in this study we used collinear **g**- and **A**-tensors, reasoning that the slight tilt of **g**- and **A**-tensors found for **1** ($\beta = 8°$) could be neglected due to the lower resolution of the broadened and split spectra[31] (see Figure 8). Chart 3 shows the orientation of the tensors' principal axes within the molecular frame. The *z*-axis for the $[Me_4dtneMn_2(\mu\text{-}O)_2]^{2+}$ core is placed perpendicular to the $Mn_2(\mu\text{-}O)_2$ plane, while the *x*- and *y*-axes lie in the direction of the Mn ions and the two μ-O groups, respectively. The *z*-direction is the unique axis for the dipolar coupling tensor between the $[Me_4dtneMn_2(\mu\text{-}O)_2]^{2+}$ core and the radical.

Complex **5** features a strongly AF coupled $Mn^{IV}Mn^{IV}$ core, yielding a core subspin $S_{Mn2}{}^0 = 0$ at low temperature (Table 2), and a tethered NIT radical, which gives the complex an overall spin $S = 1/2$ up to temperatures of about 60 K. The frozen-solution X-band spectrum of this "magnetically isolated" tethered NIT radical is presented in the Supporting Information together with its calculated spectrum (Figure S3). At the low temperature the spin density of the NIT radical is delocalized over both NO groups, seen from the ^{14}N hyperfine splitting, which indicates the presence of two equivalent N atoms. Coulometric reduction of the $Mn^{IV}Mn^{IV}$ core to $Mn^{III}Mn^{IV}$ yields $\mathbf{5^{red}}$, wherein the AF coupled $Mn^{III}Mn^{IV}$ ($S_{Mn2}{}^0 = 1/2$) core is coupled to the NIT moiety ($S_{rad} = 1/2$) similar to **6**.

Spin−Spin Interactions in Complexes 3, 4, and 6. Solid state magnetic data for complexes **3**, **4**, and **6** reveal large singlet−triplet splitting energies, Δ_{S-T}, resulting from the long-range exchange interaction between the $Mn^{III}Mn^{IV}$ cores and the tethered radicals. For complexes **3** and **6** the values of $\Delta_{S-T} = J'$ clearly exceed the EPR microwave energy at X-band ($\cong$0.3 cm^{-1}, Table 2); therefore, EPR transitions are expected to occur only within the triplet $|T\rangle$ manifold. For complex **4** (in solid state) the level scheme appears to be more involved due to the somewhat smaller Δ_{S-T} gap of about 0.6 cm^{-1}.

Here we have measured and calculated the CW-EPR X-band powder spectra in both polarizations, $\boldsymbol{B_1}\|\boldsymbol{B_0}$ and $\boldsymbol{B_1}\perp\boldsymbol{B_0}$, as well as those at S- and Q-band frequencies for complexes **3** and **4**, and recalculated those for **6**, to systematically evaluate and distinguish between dipole and exchange interactions. To this end, the full interaction Hamiltonian was taken into account for the ground state system of $|S\rangle$ and $|T\rangle$ states from $Mn^{III}Mn^{IV}$ core spin, $S_{Mn2}{}^0 = 1/2$, and the radical, $S_{rad} = 1/2$.

$$H_{pair} = \boldsymbol{S}_{rad}\cdot(\mathbf{J_d} - J'\,\mathbf{1})\cdot\boldsymbol{S}_{\mathbf{Mn2}}{}^{\mathbf{0}} + \sum\mu_B\mathbf{S}_j\cdot\boldsymbol{g}_j\cdot\mathbf{B} + \sum\boldsymbol{S}_{\mathbf{Mn2}}{}^{\mathbf{0}}\cdot\boldsymbol{A}_i\cdot\boldsymbol{I}_i, \quad j = \text{rad, Mn2; } i = \text{MnIII, MnIV} \quad (1)$$

The Hamiltonian is a restriction of the three-spin description used above to the subspace $[|S_{Mn2}{}^0, m_{Mn2}, S_{rad}, m_{rad}\rangle]$ with the addition of anisotropic (dipolar) spin coupling. The variable $\mathbf{J_d}$ denotes the traceless anisotropic coupling matrix, J' is the isotropic exchange coupling constant (equal to the singlet−triplet splitting Δ_{S-T}), and **1** is the unity matrix. ^{55}Mn hyperfine interaction was explicitly included in the simulations because of the potential influence on singlet−triplet mixing, whereas the much weaker hyperfine coupling for the organic radicals was neglected for simplicity.

Isotropic Exchange Coupling of two paramagnetic centers can be determined from the line shape of normal-mode CW-EPR spectra if its strength is of the order or less than the EPR Zeeman splitting.[4,25] Then **g**-differences of the two centers and hyperfine interaction may induce mixing of $|S\rangle$ and $|T\rangle$ wave functions, and S−T transitions can be directly observed at the energies of the exchange splitting. These are usually weak in normal-mode ($\boldsymbol{B_1}\perp\boldsymbol{B_0}$) and may virtually vanish for coupling constants higher than about 0.1 cm^{-1}. Since complexes **3**, **4**, and **6** have exchange coupling constants $|J'|$ on the order of 1 cm^{-1} and, moreover, show relatively strong parallel-mode X-band spectra, we explored the possibility of tracing their "strong" exchange splitting and S−T transitions in parallel mode. Although the S−T transitions are only slightly enhanced in parallel polarization ($\boldsymbol{B_1}\|\boldsymbol{B_0}$, selection rule "$\Delta m = 0$"), the spectra, nevertheless, may be more sensitive to exchange splitting than in normal polarization because the "$\Delta m = 1$" transitions at $g = 2$ are greatly attenuated, and much higher microwave power may be applied without saturation effects. This experimental situation is similar for the measurement of "forbidden" half-field transitions in normal mode, which are also not readily saturated due to the low transition probabilities.[32]

In Figure 6 we show a systematic series of parallel-mode powder absorption simulations for ($\boldsymbol{B_1}\|\boldsymbol{B_0}$) as a function of the

(31) Schäfer, K. O.; Bittl, R.; Lendzian, F.; Barynin, V.; Weyhermüller, T.; Wieghardt, K.; Lubitz, W. *J. Phys. Chem. B* **2003**, *107*, 1242−1250.

(32) Eaton, S. S.; More, K. M.; Sawant, B. M.; Eaton, G. R. *J. Am. Chem. Soc.* **1983**, *105*, 6560−6567.

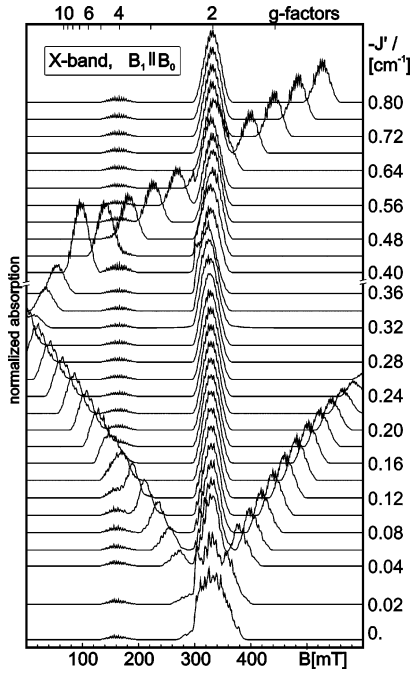

Figure 6. Simulated parallel-mode X-band EPR powder spectra ($B_1 \| B_0$) as a function of J', with $\mathbf{J_d} = (50, 50, -100) \times 10^{-4}$ cm^{-1}, and **g**- and **A**-tensor values as given in Chart 3. The microwave frequency was 9.303 GHz, and the intensities are normalized to the identical maximal amplitudes.

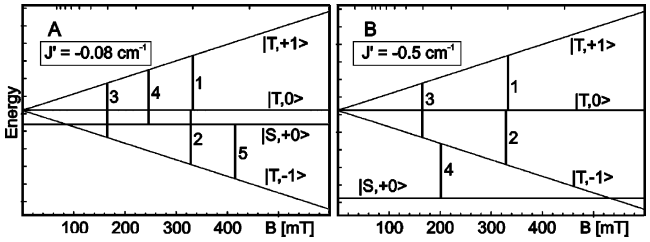

Figure 7. Energy level diagram calculated by using eq 1 without hyperfine term with $\mathbf{J_d} = (50, 50, -100) \times 10^{-4}$ cm^{-1} and $J' = -0.08$ cm^{-1} (A) and -0.5 cm^{-1} (B). The field was oriented along the direction $\theta = 45°$, $\varphi = 45°$, and the other parameters were chosen as for Figure 6. The vertical bars indicate parallel-mode EPR transitions for $\nu = 9.303$ GHz.

exchange coupling constant J' ($0 \le -J' \le 0.8$) with the anisotropic coupling matrix set to $\mathbf{J_d} = (50,50,-100) \times 10^{-4}$ cm^{-1}, corresponding to a spin−spin separation of about 7 Å in a two-point-dipole model. The **g** values and ^{55}Mn hyperfine coupling tensors used are as calculated for **1** (Chart 3).[31]

When J' is close to zero, the singlet $|S,0\rangle$ and triplet $|T,0\rangle$ levels are almost degenerate in energy and transitions are observed around $g = 2$ and at half-field at $g = 4$. The singlet and triplet states are strongly mixed due to differences in **g** values for $S_{Mn2}{}^0$ and S_{rad} and due to the Mn-hyperfine coupling (Figure 6; $0 \le -J' \le 0.02$ cm^{-1}). As the energy of $|J'|$ is increased, the $|S,0\rangle$ state is lowered in energy relative to $|T,0\rangle$, and the transitions between the $|S,0\rangle$ and $|T,-1\rangle$ and $|T,+1\rangle$ begin to move away from the $|T,-1\rangle \rightarrow |T,0\rangle$ and $|T,0\rangle \rightarrow |T,+1\rangle$ transitions at $g = 2$ (Figure 6; $0.02 \le -J' \le 0.32$ cm^{-1}). The corresponding level diagram and EPR transitions for this situation are schematically shown in Figure 7A (without hyperfine splitting). The $|S\rangle$ to $|T\rangle$ transitions 4 and 5 give rise to the J'-dependent "sidebands", analogous to the AB patterns observed in NMR spectra. Stronger exchange coupling ($-J' > 0.38$ cm^{-1}) results in $|S,0\rangle \rightarrow |T,-1\rangle$ transitions (labeled 4 in Figure 7B) that move from low to high field (from left to right)

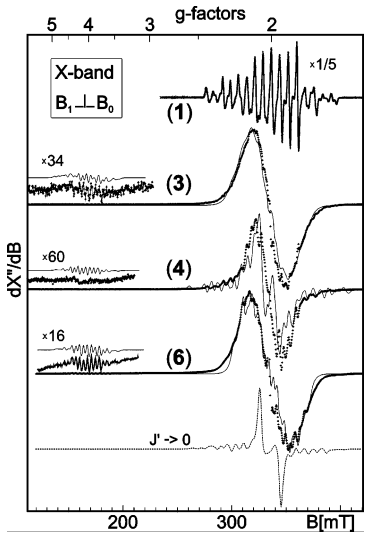

Figure 8. Normal-mode X-band EPR spectra ($B_1 \perp B_0$) of compounds **1**, **3**, **4**, and **6** in frozen CH_3CN solution. Experimental conditions (temperature, microwave power, modulation, frequency): (**1**) 30 K, 40 μW, 1.2 mT/100 kHz, 9.4348 GHz; (**3**) 10 K, 12 μW, 0.6 mT/100 kHz, 9.6259 GHz; (**4**) 10 K, 6 μW, 0.8 mT/100 kHz, 9.6224 GHz; (**6**) 10 K, 6 μW, 1.2 mT/100 kHz, 9.4217 GHz. The plots are scaled for identical g values; the field axis is given for the lowest spectrum only. The solid lines are simulations as described in the text. The bottom trace is a simulation in the limit of vanishing long-range exchange coupling ($J' = -0.01$ cm^{-1}), the anisotropic coupling is $J_{z,d} = -140 \times 10^{-4}$ cm^{-1}, $\rho = 0$. The intensity ratios $R_{4/2}$ of double-integrated half-field signals at $g = 4$ and the main signals at $g = 2$ are 2.5×10^{-4} (1×10^{-4}) for **3**; not determined for **4**, and 3.3×10^{-4} (3.5×10^{-4}) for **6** (experimental values in parentheses).

as J' is decreased (Figure 6). The intensities of the parallel-mode transitions result from field orientations away from the principal directions of **g**- and **A**-tensors, and the appearance of the spectra and relative line intensities depend on the strength of the hyperfine coupling and the anisotropic contributions $\mathbf{J_d}$. This is particularly true for the intensity of S−T transitions relative to transitions within the $|T\rangle$ manifold, which are much more intense in the parallel-mode spectra than in normal-mode spectra and, if present, are not easily missed. The absence of S−T transitions, as shown below for the experimental X-band parallel-mode spectra of the radical complexes **3**, **4**, and **6**, provides a lower limit value for J'.

Anisotropic Dipole Interaction. Half-field EPR signals at $g = 4$ arising from transitions between $|T,-1\rangle$ and $|T,+1\rangle$ levels (Figure 6) depend on the *dipolar* coupling tensor, $\mathbf{J_d}$, but not on the exchange coupling, J'.[32,33] In powder averaged normal-mode spectra ($B_1 \perp B_0$) they owe their intensity mostly to intermediate field orientations away from the principal axes of **g**- and **A**-tensors, whereas in parallel mode ($B_1 \| B_0$) the orientations close to the axes yield the major contributions.[28] Therefore, spectra recorded in both polarization modes yield complementary information about the orientation of the **g**-, **A**-, and $\mathbf{J_d}$-tensors. The overall intensity of the half-field signals in a powder average depends critically on the major component $J_{d,z}$, and moreover, the rhombicity of $\mathbf{J_d}$ ($J_{d,x} \neq J_{d,y}$) may also influence their line shapes and intensities. We recall that rhombic spin-coupling matrixes cannot arise from a basic two-point dipole interaction; however, an extended model featuring more general distributions of spin densities may yield any symmetry for $\mathbf{J_d}$. The EPR simulations for **3**, **4**, and **6** are not very sensitive

(33) Eaton, S. S.; Eaton, G. R. *J. Am. Chem. Soc.* **1982**, *104*, 5002−5003.

to the exact orientation of the $\mathbf{J_d}$-tensor, but the assignments of the main component to the *z*-, *x*-, or *y*-directions have significant effects on both signals at $g = 2$ and $g = 4$, and in this way, the basic orientation of the $\mathbf{J_d}$-tensor could be determined.

Previously it has been shown that the relative intensity of the half-field transitions has an r^{-6} (!) dependence on the separation, *r*, of point-dipole centers, independent of J'.[1,32−34] In the limit of weak exchange, where the $g = 2$ transitions are only moderately split, or in strong exchange where only triplet transitions are observed, the half-field transitions at $g = 4$ may be normalized to the full intensity of the $g = 2$ transitions. From a perturbation treatment[33,35,36] it has been shown that the intensity ratio $R_{4/2} = I(g = 4)/I(g = 2)$ follows the relation $R_{4/2} = \text{const}/r^6\nu^2$, where ν is the spectrometer frequency in GHz.[1,32] We have adapted this relation and applied it to parallel-mode spectra since relatively strong parallel-mode signals were obtained for the present complexes compared to the notoriously weak half-field signals observed in normal mode. We have calculated the intensity ratio $R_{4/2}$ for a number of parallel-mode simulations ($\boldsymbol{B_1}||\boldsymbol{B_0}$) with point-dipole separations, *r*, in the range 5 Å ≤ *r* ≤ 10 Å and fit the data to the polynomial $c{\cdot}r^n$. The best value for the exponent in the present situation was found to be $n = -5.6$, with slightly varying coefficients, *c*, for J' values in the range −0.3 to −2 cm^{-1} (see Figure S4). The experimental values[37] of $R_{4/2}$ for complexes **3**, **4**, and **6** put hard constraints on the possible solutions for $\mathbf{J_d}$ below.

Complexes 3 and 6. Our previous interpretation of the X-band EPR spectra of complex **6** was based on a spin Hamiltonian for an isolated spin-triplet manifold ($S = 1$)[38] and neglected possible level mixing or transitions between the singlet $|S\rangle$ and triplet $|T\rangle$ states. The simplification is corroborated here by a comparison of the parallel-mode EPR spectra for **6** (shown in Figure 9 trace **6**) with the simulated absorption pattern of Figure 6 which takes into account all $|S\rangle$ and $|T\rangle$ states. Experimentally, complex **6** exhibits a distinctly strong half-field signal at $g = 4$, but indications of S−T transitions cannot be detected even for field sweeps of up to 1000 mT (which would be the resonance field of S−T transitions for $|J'| \cong 1.2$ cm^{-1}). Alternatively, simulations in the weak exchange limit with $|J'| < 0.02$ cm^{-1} were also not possible for the series of spectra recorded at X-, S-, and Q-band frequencies (see also trace "$J'\rightarrow 0$" in Figures 8 and 9, bottom). We conclude, therefore, that complex **6**, in frozen solution, also exhibits relatively strong long-range exchange interaction between the $Mn^{III}Mn^{IV}$ core and the NIT radical of at least 1 cm^{-1}. Accordingly, the CW-EPR spectra of **6** at X-band in normal and parallel mode ($\boldsymbol{B_1}\perp\boldsymbol{B_0}$ and $\boldsymbol{B_1}||\boldsymbol{B_0}$) and the S- and the Q-band spectra could be consistently simulated with $J' = -1.1$ cm^{-1} taken from solid state magnetization measurements[28] (see Figures 8−10, traces **6**, solid lines). As expected, the appearance of the simulated spectra in this regime of J' is virtually insensitive to variations of the parameter. Although not all the details of the experimental spectrum with the inherent **g**-anisotropy, hyperfine interaction, and effective zero-field splitting are perfectly matched, the overall trend at three different frequencies is well reproduced with the parameters given in Table 2. Better fits may be achieved by employing sophisticated line-shape models and distributions

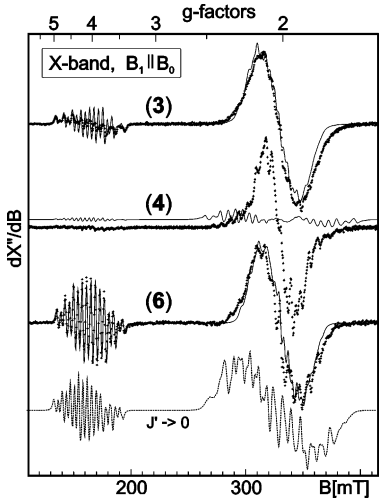

Figure 9. Parallel-mode X-band EPR spectra ($\boldsymbol{B_1}||\boldsymbol{B_0}$) of compounds **3**, **4**, and **6** in frozen CH_3CN solution. Experimental conditions (temperature, microwave power, modulation, frequency): (**3**) 6.3 μW, 0.6 mT/100 kHz, 9.3134 GHz; (**4**) 3 mW, 0.6 mT/100 kHz, 9.2977 GHz; (**6**) 20 μW, 0.8 mT/100 kHz, 9.3032 GHz. The plots are scaled for identical *g* values; the field axis is given for the lowest spectrum only. The solid lines are simulations as described in the text. The bottom trace is a simulation in the limit of vanishing long-range exchange coupling ($J' = -100 \times 10^{-4}$ cm^{-1}, $J_{z,d} = -140 \times 10^{-4}$ cm^{-1}, $\rho = 0$). The intensity ratio $R_{4/2}$ of double-integrated half-field signals at $g = 4$ and the main signals at $g = 2$ are 0.061 (0.065) for **3**; not determined **4**, and 0.087 (0.089) for **6** (experimental values in parentheses).

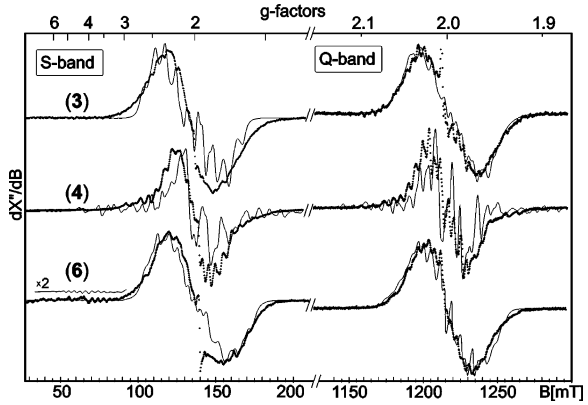

Figure 10. S-band and Q-band EPR spectra of compounds **3**, **4**, and **6** in frozen CH_3CN solution. Experimental conditions for S-band: temperature 10 K, microwave power 197 μW, modulation 0.6 mT/100 kHz, frequency (**3**) 3.8229 GHz; (**4**) 3.90226 GHz; (**6**) 3.9146 GHz, and Q-band: 50 K (25 K for **6**), microwave power 40 μW, modulation 0.6 mT/100 kHz, frequency (**3**) 34.0177 GHz; (**4**) 34.0178 GHz; (**6**) 34.0432 GHz. The plots are scaled for identical *g* values; the field axes are given for the respective lowest spectra only. The solid lines are simulations as described in the text.

(34) Pake, G. E. *Paramagnetic Resonance*; W. A. Benjamin, Inc.: New York, 1962.
(35) Boas, J. F.; Hicks, P. R.; Pilbrow, J. R. *J. Chem. Soc., Farday Trans.* **1978**, *74*, 417−431.
(36) Coffman, R. E.; Pezeshk, A. *J. Magn. Reson.* **1986**, *70*, 21−33.
(37) The experimental values for $R_{4/2} = I(g = 4)/I(g = 2)$ were obtained by numerical double-integration in the corresponding field ranges of the X-band derivative spectra. To this end, baselines were individually corrected with offset and linear slopes so that comparable absorption spectra without background were obtained that were readily integrated for the intensity determination.
(38) The approach of an isolated triplet applied in ref 28 yielded very satisfactory and accurate results for the normal-mode X-band EPR spectra from compound **6**, whereas for the parallel-mode spectra, with $B_1||B_0$, the simulations did not properly account for the intensity in the region at $g = 2$ relative to the half-field transitions at $g = 4$. We speculated that this is due to the neglected interaction of $|S\rangle$ and $|T\rangle$ states caused by competing Zeeman interaction (*g*-differences) and hyperfine interaction. However, we realized now that we had used too high thresholds for the calculation of transition probabilities. At $B_1||B_0$ condition many weak transitions between the hyperfine levels with (m_S, $m_I(1)$, $m_I(2)$) quantum numbers for the two ^{55}Mn nucleii may sum to considerable contributions. With appropriate thresholds (trpr >0.0001) now the triplet calculations yield also nice results for $B_1||B_0$, equivalent to those shown here.

of parameters; however, we chose to refrain from doing this because unique solutions are difficult to obtain and the additional gain in chemical information is marginal.

The CW-EPR spectra for complex **3**, which features a PROXYL radical, are similar to those for complex **6**, and the arguments related to the determination of the long-exchange coupling constant, J', for **6** (above) also hold for **3** (Figures 8−10, traces **3**). Apparently, the singlet−triplet gap, Δ_{ST}, in this case also exceeds the microwave energies at S- to Q-band frequencies. Therefore, simulations for complex **3** were carried out with $J' = -2.8$ cm^{-1} obtained from solid state magnetization and other parameters as given in Tables 2 and 3. The spectra of **3** and **6** differ, however, in the relative intensities of their half-field signals at X-band normal-mode and parallel-mode detection (Figures 8 and 9, note the different zoom factors for the insets of traces **3** and **6**). This indicates that **3** has a significantly *lower* anisotropic coupling compared to **6**, although the metric separation of the $Mn^{III}Mn^{IV}$ center and the radical is substantially shorter for **3**. Accurate values for the major component $J_{d,z}$ of the coupling tensor $\mathbf{J_d}$ were determined by fitting the relative integrated intensities of the half-field transitions[32,33] for the X-band spectra (Table 2). We highlight the close match in experimental and simulated half-field intensity ratios $R_{4/2}$ for **3** and **6** for both normal- and parallel-mode X-band spectra (see captions for Figure 8 and 9). The values of the rhombicity parameter $\rho = (J_{d,x} - J_{d,y})/J_{d,z}$ of $\mathbf{J_d}$ are less accurate for both compounds, as one may expect due to the relatively low resolution of the lines at $g = 2$ at the different frequencies. At Q-band frequencies the effect of anisotropic coupling (zfs) and also hyperfine interactions are weaker compared to those at X- and S-band. Overall, the X-band CW spectra appear to provide the best conditions for determining spin-coupling parameters. We estimate from the present simulations that the rhombicity of $\mathbf{J_d}$ is $\rho = 0 \pm 0.1$ for **6** and $\rho = 0.1 \pm 0.05$ for **3**. The orientation of the main axis of $\mathbf{J_d}$ in the direction of the *z*-axis for **g**- and **A**-tensors (Chart 3), or close to it, is most significant. Small rotations around the *x*- or *y*-axes with Euler angles of less than 25° are equally compatible with the experimental pattern for **6**, whereas for complex **3**, a tilt of $\mathbf{J_d}$ by $\beta = 30°$ clearly improved the quality of the simulations. The orientation properties of the coupling tensors are derived, to a large extent, from simulation of the half-field signals at $g = 4$. High-resolution half-field spectra for **3** are shown in Figure 11, while the corresponding spectra for **6** have been communicated previously.[28] The S-band spectrum for **6**, featuring identifiable and resolved half-field transitions at $g = 4$, has also been reasonably well simulated (Figure 10, bottom inset). For complexes **3** and **4** these half-field signals do not exceed the noise level. Even with more sophisticated selections of $\mathbf{J_d}$-tensors obtained from distributed-spin density models for the dipole interactions (see below), the quality of the simulations did not improve further.

The anisotropic coupling tensor $\mathbf{J_d} = (70, 70, -140) \times 10^{-4}$ cm^{-1} found for **6** is unexpectedly large when considering the metric separation between the NIT radical and the $Mn^{III}Mn^{IV}$ core; however, it is in accordance with our previous interpretation from triplet simulations.[39] The significance of the result is further demonstrated by the severe misfit simulation that is obtained with $J_{d,z} = -55$ cm^{-1} (Figure S5), which is the hypothetical value for the interaction of two point dipoles with a separation $r = 8.8$ Å. In addition, experimental factors, particularly for the parallel-mode spectra, indicate that the actual values for $\mathbf{J_d}$ are not overestimated. Even if minor "leaking" of normal-mode intensity into the parallel-mode spectrum had occurred, it would contribute mainly to the $\Delta m = 1$ signals at $g = 2$. In that case, the ratio $R_{4/2}$ would have been *underestimated*, and the true values for $\mathbf{J_d}$ of **6** would be even higher than reported. Opposite considerations apply for the determination of $\mathbf{J_d}$ for complex **3**. In that case, vanishingly small half-field signals in the *normal-mode* X-band spectra suggest that the reported value is at the *upper limit* of confidence.

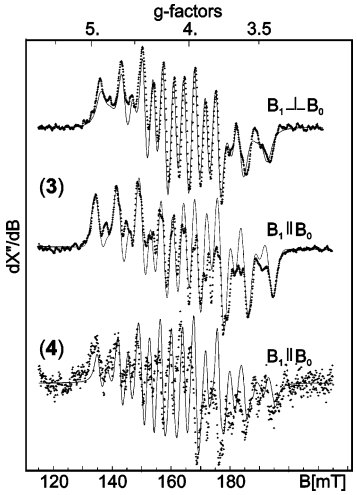

Figure 11. Half-field X-band EPR spectra in normal-mode ($\boldsymbol{B_1}\perp\boldsymbol{B_0}$) and parallel-mode ($\boldsymbol{B_1}\|\boldsymbol{B_0}$) for compounds **3** and **4** in frozen CH_3CN solution. Experimental conditions: temperature 9.8 K, modulation 0.5 mT/100 kHz, microwave power and frequency: (**3**) at ($\boldsymbol{B_1}\perp\boldsymbol{B_0}$) 5 μW, 9.6259 GHz; (**3**) at ($\boldsymbol{B_1}\|\boldsymbol{B_0}$) 20 μW, 9.3128 GHz; (**4**) at ($\boldsymbol{B_1}\|\boldsymbol{B_0}$) 20 mW, 9.29779 GHz. The plots are scaled for identical *g* values; the field axis is given for the lowest spectrum only. The solid lines are simulations as described in the text.

Finally, the half-field signals for **3** ($\boldsymbol{B_1}\perp\boldsymbol{B_0}$ and $\boldsymbol{B_1}\|\boldsymbol{B_0}$, Figure 11) prove that **g**- and **A**-components for the $Mn^{III}Mn^{IV}$ core are practically identical to those of the nonradical parent complex **1**. Since these signals are triplet $|T,-1\rangle \rightarrow |T,+1\rangle$ transitions with energies that are largely independent of exchange and dipole coupling,[33] their simulation provides independent verification for the $Mn^{III}Mn^{IV}$ local parameters.

Complex 4. The main difference in the EPR spectra of complex **4** from those of the other two radical complexes (**3** and **6**) is the almost complete absence of half-field transitions in both X-band modes (Figures 8−10, traces **4**, and Figure 11). Moreover, the total width of the observed transitions at $g = 2$ is less than that for **3** and **6**, and the lines show a different intensity distribution, with stronger resonances at the center and bell-bottomed wings. We were unable to achieve reasonable simulations of this pattern by considering only triplet transitions, i.e., strong exchange limit as with **3** and **6**. For $|J'|$ values > 0.05 cm^{-1} and any $\mathbf{J_d}$ the simulated lines at $g = 2$ showed an overall splitting that was too broad. Improvement may be achieved with reduced ^{55}Mn hyperfine interactions, but the

(39) The anisotropic coupling generates zfs of the triplet state $|T\rangle$ with a main axial *D* parameter that can be derived from the relation $D = (3/4)J_{d,z}$ if the assumption of isolated multiplets holds (ref 5). With the actual value $J_{d,z} = -140 \times 10^{-4}$ cm^{-1} for **6** one obtains $D = -105 \times 10^{-4}$ cm^{-1}, which is in reasonable agreement with previous result, $D = -90 \times 10^{-4}$ cm^{-1}, that was derived from a pure triplet analysis of the same X-band spectra (ref 28) without numerical determination of the intensity ratio $I(g = 4)/I(g = 2)$.

independent information from the resolved, optimized half-field signals recorded in parallel-mode (Figure 11) clearly shows that the local **g**- and **A**-parameters for the $Mn^{III}Mn^{IV}$ core of complex **4** are identical to those for **3** and **6** and the "parent" complex **1**. This suggests that the long-range interaction between the $Mn^{III}Mn^{IV}$ core and the tethered TEMPO radical is much weaker than for **3** and **6**. We also point out that S−T transitions similar to those depicted in Figure 6 are absent for **4**, which indicates that $|J'|$ is about 0.02 cm^{-1} or less (see Figure 9), in contrast to the exchange energy measured ($J' = -0.6$ cm^{-1}) from solid state magnetization.

A preliminary first-order perturbation simulation[40] of the X-band normal-mode spectrum, similar to that applied to the spectra of the $S_2Y_z^{\bullet}$ of PSII,[10] suggests a possible solution with $J' \approx -0.0066$ cm^{-1}, $J_{d,z} \approx -100 \times 10^{-4}$ cm^{-1} (see Figure S6). Accordingly, rather consistent simulations were obtained with the full interaction Hamiltonian (eq 1) for X-, S-, and Q-band spectra of **4** with parameter set $J' = -250 \times 10^{-4}$ cm^{-1}, anisotropic coupling tensor $J_{d,z} = -105 \times 10^{-4}$ cm^{-1}, and rhombicity parameter $\rho = 0.5$ (Figures 8−11, traces **4**). From this it is clear that complex **4** exhibits the weakest dipole coupling within our series of $Mn^{III}Mn^{IV}$/radical complexes. Although the details of the line shapes are poorly reproduced, the overall fits for the three frequencies are satisfactory, and we refrain from sophisticated line-shape models for the reasons given above even though individual spectra are easily improved, overall solutions are difficult to obtain.

Curiously, there is large disagreement between the simulation and the experimental X-band parallel mode spectrum for complex **4** (Figure 9, trace **4**). The experimental spectrum is dominated by a strong central intensity at $g = 2$, where the simulation with the above parameters yields weak signals at $g = 2$ that are spread in a wide field range. The experimental intensity distribution appears to indicate large values for J' (as for **3** and **6**), in contradiction to the normal-mode X-band and S- and Q-band spectra. We attribute the misfit of the X-band parallel-mode spectrum to possible experimental error rather than different simulation parameters. The parallel-mode spectrum of complex **4** is exceptionally weak, and a small "leak" of intensity from normal-mode into the parallel-mode spectrum would have profound consequences and may easily have occurred due to imperfections in the dual-mode cavity or slight misalignment of the electromagnet. At identical conditions of temperature, modulation, and power, the normal-mode signals of **4** are approximately 300 times stronger than the parallel-mode signals, which is more than 6 times the intensity of analogous spectra for **3** and **6**. Therefore, spurious contributions of normal-mode transitions may well be picked up in the parallel-mode measurement. By this reasoning we chose to ignore the X-band parallel-mode spectrum (Figure 9, experimental trace **4**) in simulations for complex **4**.

Distance Information. The magnetic moments of the AF coupled $Mn^{III}Mn^{IV}$ cores of complexes **3**, **4**, and **6** are distributed over both manganese centers with local contributions derived for the well-isolated magnetic ground states with subspin $S_{Mn2}{}^0 = 1/2$ from a basic spin projection technique.[30,31,41−43] Dipole interactions between such magnetic dimers and remote paramagnetic centers (radicals) are not appropriately described by a two-point dipole model.[29] The moments of the three paramagnetic (point) sites must be considered individually. This approach has been previously applied for the interpretation of EPR[9,29,44−48] and ELDOR measurements[49] of multicenter spin-coupled systems and for the calculation of hyperfine tensors in ENDOR[11,50−52] and paramagnetic NMR experiments for several complexes including **1**.[30] Here we adapt a three-spin point model for the interpretation of the anisotropic coupling tensors for complexes **3**, **4**, and **6**.

The local magnetic moments μ_1 and μ_2 of the strongly AF coupled manganese ions with ground state $S_{Mn2}{}^0 = 1/2$ are determined by the individual spin contributions $S_i = K_i \cdot S_{Mn2}{}^0$, according to the Wigner-Eckart theorem.[43] The spin projection factors are $K_1 = 2$ for Mn^{III} ($S_{MnIII} = 2$) and $K_2 = -1$ for Mn^{IV} ($S_{MnIV} = 3/2$). Dipole interaction between the $Mn^{III}Mn^{IV}$, $S_{Mn2}{}^0 = 1/2$, core and radical, $S_{rad} = 1/2$, is given by

$$H_{dipole} = (\mu_0 \mu_B^2/4\pi) \sum_{i=1,2} (g^0_{Mn2} g_{rad}/r^3_{i,rad}) K_i (S_{Mn2}{}^0 \cdot S_{rad} - 3(S_{Mn2}{}^0 \cdot r_{i,rad})(S_{rad} \cdot r_{i,rad})) \quad (2)$$

where $g_{Mn2}{}^0 = \sum_i K_i g_i$ denotes the g value of the dimanganese cluster. The total dipole interaction is represented by the sum of the coupling tensors between the two manganese ions and the respective radical, weighted by the projection factors K_i. We applied this expression to calculate anisotropic coupling tensors $\mathbf{J_d}$ using the metric parameters of the complexes **3**, **4**, and **6** obtained from X-ray diffraction data.

The single C−C bond connecting the PROXYL radical of complex **3** to its dimanganese cluster (C32−C33, Figure 1) allows rotations of the radical group around the z-axis of the spin system (Charts 1, 3). Thus, weak electronic interactions of this group with the dtne ligand and solvent in the frozen solvent matrix of the EPR sample may stabilize different configurations to those observed in crystalline state. Since the radical resides predominantly on the NO group in an off-axis position, the rotational orientation of the PROXYL residue influences the strength and symmetry properties of the dipole coupling with the $Mn^{III}Mn^{IV}$ core. To explore the situation in **3**, we performed model calculations for the expected $\mathbf{J_d}$ matrix using eq 2 for an "idealized" molecular core, as sketched in the inset of Figure 12A. The metric details were obtained from the X-ray diffraction data, and the off-axis shift of the center of the radical magnetic moment was estimated to be 2 Å (which corresponds to a localization of the spin density at the center

(40) Hore, P. J. In *Advanced EPR: Applications in Biology and Biochemistry*; Hoff, A. J., Ed.; Elsevier: Amsterdam, 1989; pp 405−438.
(41) Sands, R. H.; Dunham, W. R. Q. *Q. Rev. Biophys.* **1975**, *7*, 443.
(42) Blondin, G.; Girerd, J.-J. *Chem. Rev.* **1990**, *90*, 1359.
(43) Bencini, A.; Gatteschi, D. *EPR of Exchange Coupled Systems*; Springer-Verlag: Berlin, 1990.
(44) Guigliarelli, B.; More, C.; Fournel, A.; Asso, M.; Hatchikian, E. C.; Williams, R.; Cammack, R.; Bertrand, P. *Biochemistry* **1995**, *34*, 4781−4790.
(45) Bertrand, P.; Camensuli, P.; More, C.; Guigliarelli, B. *J. Am. Chem. Soc.* **1996**, *118*, 1426−1434.
(46) Fournel, A.; Gambarelli, S.; Guigliarelli, B.; More, C.; Asso, M.; Chouteau, G.; Hille, R.; Bertrand, P. *J. Chem. Phys.* **1998**, *109*, 10905−10913.
(47) Sanakis, Y.; Petasis, D.; Petrouleas, V.; Hendrich, M. *J. Am. Chem. Soc.* **1999**, *121*, 9155−9164.
(48) Caldeira, J.; Belle, V.; Asso, M.; Guigliarelli, B.; Moura, I.; Moura, J. J. G.; Bertrand, P. *Biochemistry* **2000**, *39*, 2700−2707.
(49) Elsässer, C.; Brecht, M.; Bittl, R. *J. Am. Chem. Soc.* **2002**, *124*, 12606−12611.
(50) DeRose, V. J.; Liu, K. E.; Lippard, S. J.; Hoffman, B. M. *J. Am. Chem. Soc.* **1996**, *118*, 121−134.
(51) Canne, C.; Ebelshauser, M.; Gay, E.; Shergill, J. K.; Cammack, R.; Kappl, R.; Hüttermann, J. *J. Biol. Inorg. Chem.* **2000**, *5*, 514−526.
(52) Randall, D. W.; Gelasco, A.; Caudle, M. T.; Pecoraro, V. L.; Britt, R. D. *J. Am. Chem. Soc.* **1997**, *119*, 4481−4491.

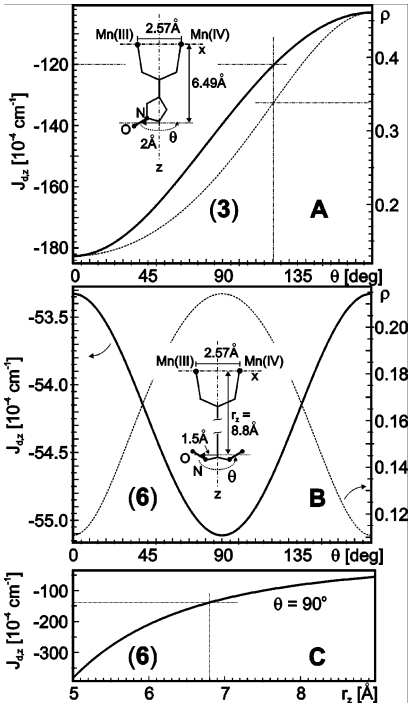

Figure 12. Theoretical values for the main component $J_{z,d}$ and the rhombicity parameter ρ of the diagonal anisotropic coupling tensor for idealized molecular cores of compounds **3** and **6** (insets) as a function rotation angle θ (A, B) and as a function of the radial separation r_z (C).

of the NO bond). The calculated $\mathbf{J_d}$-tensor was diagonalized, and the main component $J_{d,z}$ and the rhombicity parameter, $\rho = (J_{d,x} - J_{d,y})/J_{d,z}$, were plotted versus the rotation angle θ. The obtained values of $J_{d,z}$ shown in Figure 12A vary in the range from -100×10^{-4} to -180×10^{-4} cm^{-1} for the hypothetical rotational angle θ in the range 0−180°, with rhombicity parameters between $\rho = 0$ and 0.5. As expected, the strongest interaction is observed for $\theta = 0$ because this yields the shortest distance to the Mn^{III} ion, which carries the majority of the spin density for the spin-coupled dimanganese core ($K_1 = +2$). From this calculation we see that the experimental value for **3**, $J_{d,z} = -120 \times 10^{-4}$ cm^{-1} (Table 2), matches the rotation curve at the angle $\theta = 120°$, which we assign to the mean orientation of the radical moiety of complex **3** in frozen solution. The slight tilt of the calculated, nondiagonal full $\mathbf{J_d}$-tensor relative to the principal axes was not considered in this comparison as with the EPR simulations of the spectra. Therefore, the separation of the $Mn^{III}Mn^{IV}$ core and the PROXYL radical of complex **3** determined from EPR analysis is consistent with the X-ray diffraction data and provides an estimate for the molecular conformation in frozen solution.

The molecular structure of complex **4** also reveals a slight shift of the NO group in the TEMPO radical from the spectroscopic *z*-axis (Figure 1). Corresponding three-point calculations for $\mathbf{J_d}$ similar to that for **3**, with an off-axis shift of 1 Å for the center of the radical magnetic moment, also yield an angle $\theta = 120°$ for the "best" mean rotation of the TEMPO group around the *z*-axis in frozen solution at which $J_{d,z}$ matches the experimental value (-105×10^{-4} cm^{-1}). The rhombicity parameter for $\mathbf{J_d}$ at this angle is $\rho = 0.2$ (not shown). Hence, the EPR distance measurement for **4** is also consistent with the molecular structure.

The spin density of the NIT radical in compound **6** in frozen solution is symmetrically distributed over both NO groups, as inferred from the EPR spectra of the related complex **5** with diamagnetic dimanganese core (Figure S3). In this case, eq 2 has been modified to include two manganese ions and two radical magnetic point centers. The solid line in Figure 12B shows the variations of $J_{d,z}$ for rotations of the NIT group around the *z*-axis, when the off-axis shift of the radical spin partitions on the two NO groups are taken to be 1.5 Å and the separation from the Mn_2 core in the *z*-direction is set to $r_z = 8.8$ Å (from the X-ray diffraction data). Interestingly, the calculated range of $J_{d,z}$ is remarkably small, with a maximum value of -55×10^{-4} cm^{-1} at $\theta = 90°$, which is very similar to a rough estimate from the basic two-point model for $r = 8.8$ Å ($J_{d,z} = -50.5 \times 10^{-4}$ cm^{-1}). This is substantially lower than the experimentally determined result, $J_{d,z} = -140 \times 10^{-4}$ cm^{-1}, and absolutely inconsistent with experiment (see Figure S5 for a simulation of the X-band spectrum of **6** with $J_{d,z} = -55 \times 10^{-4}$ cm^{-1}). Apparently, the effective mean separation of the magnetic moments is significantly *smaller* than the metric separation of the manganese ions and the NO groups. The calculated distance dependence of $J_{d,z}(r_z)$ at the optimal rotation angle $\theta = 90°$ (Figure 12C) suggests a maximum mean effective separation in the *z*-direction of $r_z = 6.5$ Å (structurally 8.8 Å). These discrepancies lead one to conclude that either (a) the large anisotropic coupling of complex **6** is not of pure dipole origin but comprises contributions from anisotropic exchange or (b) the spin of the NIT radical is not well centered on the NO groups. We are inclined to believe that a minor fraction of the radical spin density *is* delocalized onto the phenyl ring toward the dimanganese core, which due to the r^{-3} dependence of the dipole interaction, effectively shifts the center of the radical magnetic moment and substantially obscures the interpretation of the EPR data for **6**.

Conclusions

The series **1**−**6** represent an interesting family of closely related dimanganese complexes with a rich redox chemistry. They all contain the $[(Me_4dtne)Mn_2(\mu\text{-}O)_2(\mu\text{-}O_2XR)]^n$ core with different organic residues, R, tethered to the dimanganese core through carboxylate, X = C, or boronate, X = B, bridges. By attaching nitronyl nitroxide (NIT), TEMPO, or PROXYL groups, we have obtained complexes with radical residues at different distances to the dimanganese core and with different π- and σ-pathways for through-bond exchange. Electrochemically, the dimanganese cores may adopt three reversible valence states, $Mn^{III}Mn^{III}$, $Mn^{III}Mn^{IV}$, and $Mn^{IV}Mn^{IV}$, with energetically well-isolated subspin ground states $S_{Mn2}{}^0 = 0$, 1/2, and 0, respectively. The μ-boronate or μ-carboxylate bridges show no observable differences for the exchange mechanism or spin density distribution at the manganese centers.

Complexes **3**, **4**, and **6** show long-range exchange between the $S_{Mn2}{}^0 = 1/2$ spin of the $Mn^{III}Mn^{IV}$ cores and the $S_{rad} = 1/2$ spin on the radical moieties. In the solid state the strongest isotropic interaction is found for the PROXYL complex **3** ($J' \approx -3$ cm^{-1}) with the shortest distance ($r = 6.9$ Å), whereas the weakest exchange is observed for the TEMPO derivative **4** ($J' \approx -0.6$ cm^{-1}) at intermediate distance ($r = 7.7$ Å). These results are somewhat unexpected since both the PROXYL and the TEMPO groups contain similar single bonds and σ-interac-

tions in their connections to the dimanganese core, while the NIT-radical moiety of complex **6** ($r = 8.8$ Å) has a conjugated π-system, which is expected to mediate long-range superexchange and spin polarization.

Others have noted that the exchange between nitroxide spin labels, including TEMPO and PROXYL groups, and transition metal complexes is usually weak and hardly exceeds 0.5 cm^{-1}.[25−27] An exception is found in the substantial long-range exchange interaction for pyridine-substituted NIT radicals and Mn^{II} ions (bound through the pyridyl nitrogen).[53,54] In this case, ferro- as well as antiferromagnetic coupling has been measured from solid samples with coupling constants on the order of 5 cm^{-1} (converted to the notation $H = -2JS_1S_2$). The authors[53] argue that the magnetic orbital of the pyr-NIT group shows sizable spin density at the coordinating pyridine nitrogen. By similar reasoning for compound **6** we may expect some radical spin density at the bridging C atom of the NIT-containing ligand (μ-O_2CPhNIT), which apparently has nonvanishing overlap with the magnetic orbitals of the dimanganese core. This can be rationalized from the $3d(t_{2g})^3$ and $3d(t_{2g})^3(e_g)^1$ electronic configurations of Mn^{IV} and Mn^{III} ions with basically elongated octahedral geometry. The apical oxygen ligands in the *z*-positions at both manganese sites can acquire spin density due to π-interaction with the unpaired electrons in the d_{zx} and d_{yz} magnetic orbitals and in turn transmit it through their π_x* and π_y* orbitals to the bridging carbon (or boron) atom. Since the local moments at Mn^{III} and Mn^{IV} are markedly different due to spin vector coupling ($K_1 = 2$, $K_2 = -1$), there is sizable asymmetry and a nonvanishing difference of α- and β-spin density from the dimanganese core at the bridging carbon atom. This may overlap with the spin density contribution from the radical for most arbitrary orientations of the NIT group (or other radicals in other cases). The effect is further enhanced through the "σ-channel" due to σ-interaction of the bridging carboxylate oxygen with the d_{z^2} orbital of Mn^{III} (which carries majority (α) spin density from the cluster). The fact that substantial superexchange on the order of a few wavenumbers can be mediated between the NO group of the PROXYL moiety of **3** and the dimanganese core demonstrates the effectiveness of this σ-channel. Thus, single bonds do not necessarily block or weaken exchange pathways, which may have consequences for the assessment of long-range interactions in biological systems.

The long-range coupling observed for complex **4** in the solid state (-0.6 cm^{-1}) virtually disappears in (frozen) solution. At present we cannot exclude that weak *intermolecular* interactions might have contributed and obscured the measurements of solid **4**. However, it is remarkable that the isolated complex in solution shows a more than 2 orders of magnitude weaker long-range exchange between the dimanganese core and the TEMPO radical ($|J'| \approx 0.025$ cm^{-1}) than complex **3** with PROXYL, although both have similar intramolecular covalent linkages. The difference appears to be related to the propagation of spin density through the five- and six-membered rings that carry the NO radicals in PROXYL and TEMPO, respectively.

The anisotropic spin coupling between the dimanganese core and tethered radical in complexes **3**, **4**, and **6** is on the order of -100×10^{-4} cm^{-1}, which gives rise to significant EPR line splittings of approximately 10 mT and sizable half-field transitions, particularly in parallel-mode detection. Therefore, line shape simulations of CW spectra offer high sensitivity for detecting this interaction. In contrast, preliminary experiments with pulsed ELDOR techniques reveal prohibitively short response times for the spin systems. For the interpretation of the anisotropic spin coupling we may safely assume that for complexes **3**, **4**, and **6** it is of predominantly dipole origin. Applying the relation of Moriya, $(\Delta g/g)^2 J'$, or even more sophisticated estimates[38] to the low *g*-anisotropy $\Delta g \cong 0.01$ and weak isotropic exchange of less than $\cong -3$ cm^{-1} limits the possible anisotropic exchange contributions to negligibly small values for the present systems of less than a few 10^{-4} cm^{-1}. In addition, a distinct local spin density distribution must be considered and at least a three-spin dipole model must be applied to derive reliable distance information from the anisotropic coupling constants. This model yields reliable information for the anisotropic coupling in the nitroxide radical systems of complexes **3** and **4**, demonstrating the importance of accurate knowledge of spin density distribution and relative orientation of the interacting paramagnets.

This model for distance measurement from EPR data broke down for complex **6**, which shows an unexpectedly short "effective" separation between the radical and the dimanganese core. The most plausible explanation is a substantial delocalization of the radical spin density toward the cluster. Due to the r^{-3} distance dependence of the dipole−dipole interaction, even a minor fraction of the spin density may induce substantially stronger coupling than a localized magnetic moment. In relation to the situation present in the $S_2Y_z^\bullet$ state of PSII we see that for systems such as **3** and **4** good models for variation in anisotropic coupling to distance are found, but for situations where substantial delocalization of the paramagnets occur, as in **6**, the situation becomes more complicated. Consequences may pertain to the infinitely more complex PSII system where, in the $S_2Y_z^\bullet$ state, the two interacting paramagnets are a four-manganese cluster of unknown magnetic geometry around which spin density may be delocalized and a tyrosyl radical of unknown orientation, which may also feature delocalization of the radical due to conjugation.

Acknowledgment. We thank Prof. R. Bittl for stimulating discussions on the interpretation of dipole couplings. The Fond der Chemischen Industrie is acknowledged for financial support, and D.M. is grateful for a stipend from the Max-Planck Society.

Supporting Information Available: A schematic view of the ligand system, syntheses (complexes **2**−**5**),[55] and data collection conditions and equipment for magnetic and EPR and electrochemistry. Simulation software for magnetic[56] and EPR[57] data and X-ray crystallographic data[58,59] in CIF format, spectroelectrochemical data for **2** and **5**, plots of the temperature dependence of the effective magnetic moments of **2** and **5**, the X-band EPR spectrum of the NIT radical of **5** in frozen matrix,

(53) Fettouhi, M.; Khaled, M.; Waheed, A.; Golhen, S.; Ouahab, L.; Sutter, J.-P.; Kahn, O. *Inorg. Chem.* **1999**, *38*, 3967−3971.
(54) Caneschi, A.; Ferraro, F.; Gatteschi, D.; Rey, P.; Sessoli, R. *Inorg. Chem.* **1990**, *29*, 4217−4223.
(55) Ullmann, E. F.; Osiecki, J. H.; Boocock, D. G. B.; Darcy, R. *J. Am. Chem. Soc.* **1972**, *94*, 7049−7059.
(56) Krebs, C.; Birkelbach, F.; Staemmler, V.; Bill, E. Simulation Program *JULIUS*; Ruhr-Universität Bochum und MPI-BAC Mülheim, 2000.
(57) Hanson, G. R.; Gates, K. E.; Noble, C. J.; Griffin, M.; Mitchell, A.; Benson, S. *J. Inorg. Biochem.* **2004**, *98*, 903−916.
(58) *ShelXl97*; Siemens Analytical X-Ray Instruments, Inc.
(59) *ShelXTL* V.5; Siemens Analytical X-Ray Instruments, Inc.

the intensity variations of half-field signals relative to signals at $g = 2$ for simulated parallel-mode spectra as a function of the separation of two point dipoles, an alternative simulation of the parallel-mode X-band spectrum of **6** with parameters as for two point-dipoles at $r = 8.8$ Å, and an alternative simulation of the normal-mode X-band spectrum of weakly coupled **4** with first-order perturbation treatment. This information is available free of charge via the Internet at http://pubs.acs.org.

JA042655W